

Deep Non-rigid Structure-from-Motion: A Sequence-to-Sequence Translation Perspective

Hui Deng¹, Tong Zhang², Yuchao Dai^{1*}, Jiawei Shi¹, Yiran Zhong^{3,5}, and
Hongdong Li⁴

¹ School of Electronics and Information, Northwestern Polytechnical University

² School of Computer and Communication Sciences, EPFL

³ SenseTime Research

⁴ Australian National University

⁵ Shanghai AI Laboratory

Abstract. Directly regressing the non-rigid shape and camera pose from the individual 2D frame is ill-suited to the Non-Rigid Structure-from-Motion (NRSfM) problem. This *frame-by-frame* 3D reconstruction pipeline overlooks the inherent spatial-temporal nature of NRSfM, *i.e.*, reconstructing the whole 3D sequence from the input 2D sequence. In this paper, we propose to model deep NRSfM from a *sequence-to-sequence* translation perspective, where the input 2D frame sequence is taken as a whole to reconstruct the deforming 3D non-rigid shape sequence. First, we apply a shape-motion predictor to estimate the initial non-rigid shape and camera motion from a single frame. Then we propose a context modeling module to model camera motions and complex non-rigid shapes. To tackle the difficulty in enforcing the global structure constraint within the deep framework, we propose to impose the union-of-subspace structure by replacing the self-expressiveness layer with multi-head attention and delayed regularizers, which enables end-to-end batch-wise training. Experimental results across different datasets such as Human3.6M, CMU Mocap and InterHand prove the superiority of our framework. The code will be made publicly available.

Keywords: Non-rigid Structure-from-Motion, Self-attention, Sequence-to-sequence translation, Temporal encoding, Self-expressiveness

1 Introduction

Non-rigid structure-from-motion (NRSfM) aims at reconstructing the 3D shape of deforming objects from multiple 2D images, which is a central topic in geometric computer vision. It is well-known that NRSfM is an under-constrained (ill-posed) problem, thus various constraints on camera motions and non-rigid shapes have been introduced to provide regularizations for the problem, such as shape basis (*e.g.* single subspace [11], union-of-subspaces [44]), trajectory basis [5], shape-trajectory [33], and temporal smoothness priors [19]. It is worth noting that all of these constraints need to be enforced over the **whole sequence** rather than in a **single-frame** manner.

* Yuchao Dai is the corresponding author (daiyuchao@gmail.com).

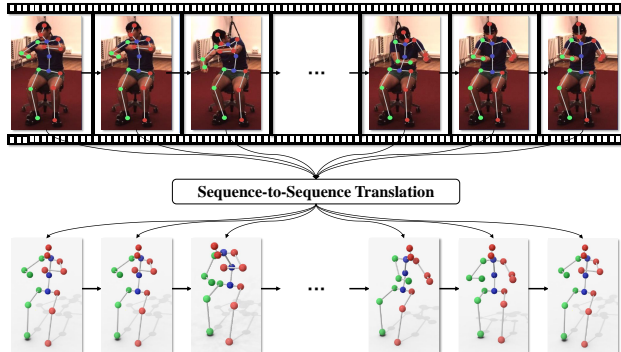


Fig. 1. A conceptual illustration of our sequence-to-sequence NRSfM reconstruction framework, where we take the 2D frame sequence as a whole to predict the deforming 3D shape sequence.

Recently, deep neural networks have been applied to the NRSfM task and have shown an improved 3D reconstruction performance in terms of both accuracy and inference speed [13,28,23]. However, most of these existing deep NRSfM methods perform non-rigid shape reconstruction from 2D observations in a *frame-by-frame* manner, overlooking the aforementioned *whole sequence* constraints that have been exploited by traditional methods for decades. As a result, their 3D non-rigid reconstructions do not always conform to the non-rigid deformation modeling.

There are two kinds of properties/constraints that are widely used in the traditional NRSfM methods: temporal smoothness of the deforming shape sequence [15,3] and low rank constraint of complex non-rigid shapes [16,44]. However, applying these constraints to the whole sequence in the deep neural networks framework is not straightforward. The main challenges are: **1)** The existing single frame based non-rigid reconstruction methods are hampered by the fact that expressing the whole sequence restrictions necessitates accepting the entire sequence as input; **2)** The motion ambiguity undermines the non-rigid shapes’ representation; **3)** The scalability issue [42] in the self-expressiveness layer [21] further makes it difficult to be fitted in the framework in an end-to-end manner.

Inspired by the sequence-to-sequence model in machine translation, we propose to solve NRSfM from a sequence-to-sequence translation viewpoint, where a 2D sequence is “translated” into a 3D sequence. From this perspective, our *sequence-to-sequence* reconstruction framework takes the input 2D sequence as a whole to reconstruct the deforming 3D non-rigid shape sequence. First, to minimize the motion ambiguity, a shape-motion predictor is applied to estimate the initial 3D shape and camera motion from a single frame before merging the entire 2D sequence features. Then, a context modeling module to model 3D shape sequence by exploiting the inherent structure within the whole sequence is adopted to enforce the subspace constraint. Specifically, to tackle the diffi-

culty in applying the union-of-subspace structure within the deep framework, we propose to replace the self-expressiveness layer with multi-head attention and delayed regularizers, which enables the end-to-end batch-wise training. For the sake of completeness, we prove the uniqueness of the reshuffled non-rigid shape [16] and show its advantage in enforcing the union-of-subspace constraint in the deep neural networks framework. Experimental results on different non-rigid datasets such as Human3.6M, CMU Mocap and InterHand demonstrate the superiority of our proposed framework.

Our main contributions are summarized as below:

- We propose a sequence-to-sequence translation perspective to deep NRSfM, where the input sequence is taken as a whole to reconstruct the 3D non-rigid shapes. This is a paradigm shift to the current deep NRSfM pipeline.
- We introduce a new way of imposing the union-of-subspace structure by replacing the self-expressiveness layer with multi-head attention and delayed regularizers, which enables the end-to-end batch-wise training.
- Our method achieves state-of-the-art performance across multiple benchmarks compared against traditional and deep NRSfM methods, showing the superiority of our method in dealing with sequential data.

2 Related Work

Here, we briefly review traditional and deep NRSfM methods, and related work in sequence-to-sequence processing.

Traditional NRSfM Methods Aiming at recovering both the deforming 3D shapes and camera motion from 2D measurements, non-rigid structure-from-motion (NRSfM) is highly ill-posed. Thus various constraints either on the camera motions or on the 3D shapes have been introduced to regularize the problem. In 2000, Bregler *et al.*[11] proposed to represent the deforming 3D shapes as a linear combination of a small number of basis shapes, *i.e.*, a low-rank subspace representation. Later, Xiao *et al.*[39] showed that there is further ambiguity in the shape basis representation. Akther *et al.*[5] introduced the DCT bases in the trajectory space. Torresani *et al.*[36] add a constraint on the shape distribution by introducing hierarchical prior. Simon *et al.*[33] unified shape and trajectory models by introducing the Kronecker-Markov prior. Dai *et al.*[16] enforced the low-rank prior on the reshuffled shape representation, thus achieving prior-free reconstruction. Besides the above single subspace based representation, the union-of-subspace representation has been used to model complex non-rigid shapes [44,1]. Besides the above sparse non-rigid reconstruction methods, there are recent efforts in achieving dense reconstruction by exploiting the spatial constraints. Garg *et al.*[18] introduced the Total Variation norm into the model to constrain dense features. Kumar *et al.*[25] performed subspace clustering in the trajectory space to achieve segmentation between different objects. At present, many methods of processing multiple NRSfM are based on image segmentation [2,25,26].

Deep NRSfM Methods Recently, deep models have been introduced to solve NRSfM [7,40,38,32]. Novotny *et al.*[28] proposed a concept of shape structure called transversal property, and designed a deep model combining canonicalization network and factorization network to rebuild camera motion and non-rigid shape. Kong *et al.*[23] used sparse dictionary learning by introducing block sparsity prior to build a multi-layer network structure to rebuild the 3D structure, which has also been extended to the perspective projection model to reconstruct the field scene [37]. To eliminate the ambiguity between camera motion and non-rigid deformation, Park *et al.*[30] used the Procrustean regression [29] to model canonical shape [30]. Very recently, Zeng *et al.*[41] proposed to use the Residual-Recursive Network and pairwise regularization to reconstruct and further regularize the reconstruction results.

Sequence Modeling Sequence to sequence modeling is originally proposed by Ilya *et al.* [35] for Neural Machine Translation and then has been widely applied to speech recognition [6], video captioning [43], action recognition [14], human body pose estimation [22] and *etc.* In this paper, we introduce the concept of sequence-to-sequence translation to NRSfM, where a 2D sequence is fluently translated to its 3D counterpart.

Uniqueness of Our Contribution Different from existing deep NRSfM methods, we solve NRSfM from a new sequence-to-sequence translation perspective, where the input sequence is taken as a whole to reconstruct the deforming 3D non-rigid shapes. In this way, existing domain knowledge in modeling NRSfM such as union-of-subspace representation, rank minimization *etc.* could be incorporated into the deep framework naturally, which is a paradigm shift from the current frame-to-frame pipeline.

3 Method

In this section, we provide the technical details of our proposed method. We start by recapping the commonly used constraints in NRSfM and then show how we implement them in our sequence-to-sequence translation framework. A theoretical proof is also provided to prove the validness of our design.

3.1 Problem Formulation and A Recap

Non-rigid structure-from-motion aims at recovering the 3D deformable shape $\mathbf{S}_i \in \mathbb{R}^{3 \times P}$ and the corresponding camera motion $\mathbf{R}_i \in \mathbb{R}^{2 \times 3}$ from 2D measurements $\mathbf{W}_i \in \mathbb{R}^{2 \times P}$ such that $\mathbf{W}_i = \mathbf{R}_i \mathbf{S}_i$. Specifically, let's stack all the F frames of 2D measurements and all the P points in a matrix form, we reach:

$$\mathbf{W} = \begin{bmatrix} \mathbf{R}_1 \mathbf{S}_1 \\ \vdots \\ \mathbf{R}_F \mathbf{S}_F \end{bmatrix} = \begin{bmatrix} \mathbf{R}_1 & & \\ & \ddots & \\ & & \mathbf{R}_F \end{bmatrix} \begin{bmatrix} \mathbf{S}_1 \\ \vdots \\ \mathbf{S}_F \end{bmatrix} = \mathbf{R} \mathbf{S}, \quad (1)$$

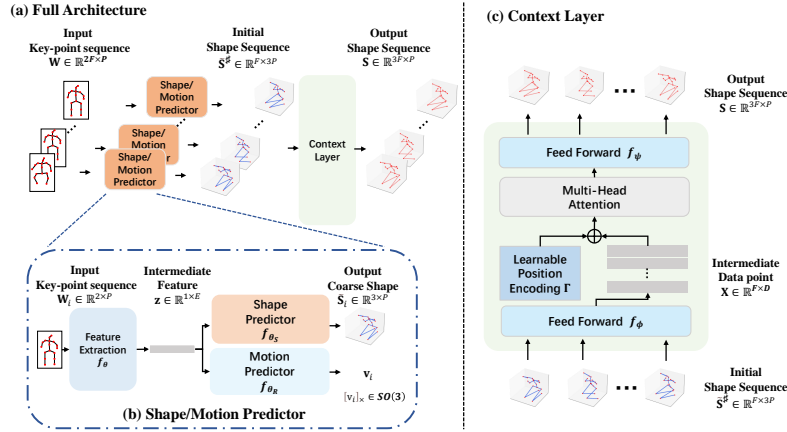


Fig. 2. An overview of our sequence-to-sequence NRSfM framework. Our framework consists of two core modules: Shape/Motion predictor (b) for estimating the initial 3D shape and camera motion from a single frame, and Context Layer (c) for adjusting the 3D shape sequence by exploiting the inherent structure within the whole sequence

where $\mathbf{R} = \text{blkdiag}(\mathbf{R}_1, \dots, \mathbf{R}_F) \in \mathbb{R}^{2F \times 3F}$ expresses the camera rotation matrix. To regularize the problem, various constraints have been introduced on the non-rigid shapes \mathbf{S}_i and camera motion \mathbf{R}_i . In Bregler’s seminal work [11], each non-rigid shape is represented in a single subspace, *i.e.*, $\mathbf{S}_i = \sum_{j=1}^K c_{ij} \mathbf{B}_j$. This single subspace representation could be naturally relaxed as minimizing the rank of the recovered shape \mathbf{S} . Later the single subspace model has been extended to the union-of-subspace representation [25,44], where the shape resides in each subspace could be expressed with shapes in the same subspace. Self-expressiveness has been used as one of the most widely used technique to implement the union-of-subspace representation, in particular, $\mathbf{S} = \mathbf{S}\mathbf{C}$.

3.2 Framework Overview

As illustrated in Fig. 2, our sequence-to-sequence deep NRSfM framework consists of two modules: **1)** non-rigid shape and motion predictor; and **2)** context modeling to regularize the sequence. It takes the input 2D sequence as a whole to predict the 3D sequence output. First, we employ a non-rigid shape and motion predictor to generate initial 3D shape and camera motion from the 2D frame. Then, the non-rigid shapes are optimized within our proposed context modeling layer to exploit the union-of-subspace representation and temporal smoothness constraint.

The entire pipeline is fully self-supervised, *i.e.*, no requirements of the ground truth camera motion and the non-rigid shape. Our method naturally builds upon the best of the two worlds, *i.e.*, learning a single frame shape and motion predictor, and enforcing the spatial-temporal constraints on the whole sequence.

3.3 Shape and Motion Prediction

One of the advantages of a deep neural network is that it can learn a good initial coarse 3D shape estimation from the training data. Given 2D input $\mathbf{W} \in \mathbb{R}^{2F \times P}$, we first encode the 2D shape by a feature extractor $f_{\theta_e} : \mathbb{R}^{2P} \rightarrow \mathbb{R}^E$ as shown in Fig. 2. Then we design a shape predictor $f_{\theta_s} : \mathbb{R}^E \rightarrow \mathbb{R}^{3P}$ and a motion feature predictor $f_{\theta_r} : \mathbb{R}^E \rightarrow \mathbb{R}^3$ to estimate a coarse estimation of 3D shapes and recover the rigid motion for each input 2D frame. The coarse reshuffled shape $\tilde{\mathbf{S}}^\#$ and its corresponding rotation \mathbf{R} are predicted as:

$$\mathbf{v}_i = f_{\theta_r}(f_{\theta_e}(\mathbf{W}_i)), \quad (2)$$

$$\tilde{\mathbf{S}}_i^\# = f_{\theta_s}(f_{\theta_e}(\mathbf{W}_i)). \quad (3)$$

To keep $\mathbf{R} \in \text{SO}(3)$, we apply the Rodrigues' rotation formula to the extracted vector \mathbf{v}_i as: $\mathbf{R}_i = \exp([\mathbf{v}_i]_\times)$, where $[\cdot]_\times$ denotes the cross-product.

3.4 Sequence Modeling and Self-expressiveness

Modeling Complex Non-rigid Motions. As analyzed in the classic NRSfM methods, complex nonrigid motion usually contains multiple primitives or simple actions. Following [25,44], we exploit the structure of the scenes along the temporal direction to compactly represent complex non-rigid scenes, but within the *deep framework*. Specifically, we represent the 3D non-rigid deformations as lying in a union of subspaces along the temporal direction. However, little has been done in incorporating the concept of union-of-subspace to a deep learning framework. Firstly, the self-expressiveness layer aims to reconstruct a signal itself by using a linear combination of other signals [21], which critically relies on the data fidelity term, namely the reconstruction error. Secondly, the regularizer term, such as the ℓ_1 or ℓ_2 norm, needs to be tuned for different batches, which makes it hard to apply on batch training.

In this paper, we propose to replace the self-expressiveness representation with a multi-head attention (MHA) block to impose the union-of-subspace underlying model. Thus, we have

$$\mathbf{S} = f_\psi(\text{MHA}(\mathbf{X})), \quad (4)$$

where $f_\psi : \mathbb{R}^D \rightarrow \mathbb{R}^{3P}$ is a residual block and MHA denotes the multi-head attention module:

$$\text{MHA}(\mathbf{X}) = \text{Concat}(\text{head}_1(\mathbf{X}), \dots, \text{head}_h(\mathbf{X}))\mathbf{W}_O, \quad (5)$$

$$\text{head}_i(\mathbf{X}) = \text{softmax}\left(\frac{\mathbf{X}\mathbf{W}_i^Q \cdot \mathbf{W}_i^{K\top} \mathbf{X}^\top}{\sqrt{D}}\right) \mathbf{X}\mathbf{W}_i^V, \quad (6)$$

where $\mathbf{W}^K, \mathbf{W}^Q, \mathbf{W}^V$ are the fully connected layer for key, query, and value, and \mathbf{W}_O is the output linear layer. Thus, the self-expressiveness layer is replaced by the softmax operation, which provides us sparse coefficients without constraints on the reconstruction error. Our recovered shapes will be obtained through performing one more feed-forward network after linear combination.

Modeling Temporal Encoding. The above self-attention representation and the union-of-subspace representation encode the complex non-rigid motion while failing to capture the essential temporal constraints. Specifically, a non-rigid shape \mathbf{S} before and after a random permutation \mathbf{PS} does not change the cost. As a result, when encoding a sequence of frames into a latent vector, the overlapping neighboring sequence tends to share a similar representation despite that the deformed shapes could be repeated in long-range. This kind of temporal smoothness has also been explored in the classic NRSfM methods. Here, we propose to incorporate the temporal information into the feature vectors so that the feature vectors can be represented by the latent vectors of temporal dependency.

Inspired by recent advances in the Transformers, such as BERT [17] and GPT [31], we design our temporal encoding to exploit the temporal smoothness constraint. Following the existing protocols, where they first encode the feature of words or image patches, we encode our coarse 3D shapes by a feedward network $f_\phi : \mathbb{R}^P \rightarrow \mathbb{R}^D$ as shown in Fig. 2 (b), followed by adding the temporal encoding feature:

$$\mathbf{X} = f_\phi(\tilde{\mathbf{S}}^\#) + \mathbf{\Gamma}, \quad (7)$$

where $\mathbf{\Gamma}$ is the temporal encoding vector. Although the design of positional encoding in NLP does not match the nature of 3D non-rigid shape sequence, *e.g.* a series of shapes could appear in a revert order but it rarely happens in NLP, they have certain similarities, for example, neighboring shapes or words are almost always together. As a result, we begin our temporal encoding in a similar manner, and it takes the form:

$$\mathbf{\Gamma}(t, 2i) = \sin(t/10000^{2i/D}), \quad \mathbf{\Gamma}(t, 2i + 1) = \sin(t/10000^{2i+1/D}). \quad (8)$$

where t is the frame number, i is the index of the latent vector, and D is the dimensionality of the feature vector. Note that $\mathbf{\Gamma}$ here is learnable and will be updated along with the networks' parameters.

3.5 Shape Regularizer

Since the reconstruction term has been removed in the MHA module, the constraints need to be addressed to avoid trivial solutions. Instead of imposing the constraint on the latent code as subspace clustering [21], we apply the regularizer after decoding the latent code to 3D shapes, where the 3D shapes' properties can be fully utilized.

First of all, we calculate the reprojection error between the estimation \mathbf{RS} result and the input \mathbf{W} to enforce the network to learn how to estimate the shape as well as the motion from the input:

$$\mathcal{L}_{\text{data}} = \frac{1}{F} \sum_i^F \|\mathbf{W}_i - \mathbf{R}_i \mathbf{S}_i\|_l. \quad (9)$$

Meanwhile, for the global shape constraint, we penalize the nuclear norm of the reshuffled shape matrix $\mathbf{S}^\# \in \mathbb{R}^{F \times 3P}$ as the nuclear norm is known as

the convex envelope of the rank function:

$$\mathcal{L}_{\text{norm}} = \|\mathbf{S}^\sharp\|_*. \quad (10)$$

It is worth noting that we are using the reshuffled shape matrix \mathbf{S}^\sharp rather than \mathbf{S} as there exists an inherent per-frame rotation ambiguity in non-rigid 3D reconstruction, *i.e.*, $\mathbf{W}_i = \mathbf{R}_i \mathbf{S}_i = \mathbf{R}_i \mathbf{Q}_i \mathbf{Q}_i^{-1} \mathbf{S}_i$, $\mathbf{Q}_i \in \text{SO}(3)$. The low-rank condition does not change as $\text{rank}(\mathbf{S}) = \text{rank}(\mathbf{Q}^{-1} \mathbf{S})$, where $\mathbf{Q} = \text{blkdiag}(\mathbf{Q}_1, \dots, \mathbf{Q}_F) \in \mathbb{R}^{3F \times 3F}$. It shows the limitation of \mathbf{S} in enforcing the low-rank constraint, *i.e.*, it cannot distinguish the non-rigid shapes from their per-frame rotated version.

In [16], Dai *et al.* introduced the reshuffled shape representation $\mathbf{S}^\sharp \in \mathbb{R}^{F \times 3P}$, which connects to \mathbf{S} as $\mathbf{S}^\sharp = g(\mathbf{S}) = [\mathbf{P}_X \ \mathbf{P}_Y \ \mathbf{P}_Z](\mathbf{I}_3 \otimes \mathbf{S})$, where $g(\cdot)$ denotes the reshuffle operation to the nonrigid shape. $\mathbf{P}_X, \mathbf{P}_Y, \mathbf{P}_Z$ are row-selection matrices defined in [16]. Based on this operator, Dai *et al.* [16] presented the block-matrix method and showed the superiority of this reshuffled shape representation over the original one. Here we analyze the role of reshuffled shape in recovering low-rank structure.

Theorem 1. *Suppose that a deformable shape $\mathbf{S}^\sharp \in \mathbb{R}^{F \times 3P}$ lies in a low-rank space, then we have:*

$$\text{rank}(g(\mathbf{S})) = \text{rank}(\mathbf{S}^\sharp) \leq \text{rank}(g(\mathbf{Q}^{-1} \mathbf{S})). \quad (11)$$

*The equal sign holds if and only if \mathbf{Q} contains only one rotation component $\mathbf{Q}_1 = \dots = \mathbf{Q}_F$, *i.e.*, a global rotation on all the frames.*

Due to space limitation, we provide complete proof and in-depth analysis in the supplemental materials. It is worth noting that Theorem 1 but the effect of Rotation Ambiguity in recovering the structure using low-rank constraint. Theorem 1 states that the rotation ambiguity \mathbf{Q} affects the rank of the reshuffled shape \mathbf{S}^\sharp directly⁶. If and only if the correct rotations are recovered (up to a global rotation), the rank of the reshuffled shape \mathbf{S}^\sharp is minimized. Therefore, we can recover the unique low-rank deformable shape using the rank minimization approach. Within our proposed deep NRSfM framework, we employ the reshuffled shape representation.

Furthermore, to ensure the uniqueness of the estimation results, we follow the *Lemma 1* of C3dpo [28] that a set of shape has the property of transversal, if there exists a canonicalization mapping $\Psi: \mathbb{R}^{3 \times P} \rightarrow \mathbb{R}^{3 \times P}$ that could eliminate all rigid motion in shape \mathbf{S} , and the processed \mathbf{S} is consistent with the original \mathbf{S} , thus for any random rotation $\mathbf{R} \in \text{SO}(3)$, we always have $\mathbf{S} = \Psi(\mathbf{R}\mathbf{S})$. If shapes in the output shape sequence do not contain various rigid motions, the ambiguity caused by the camera motion is eliminated, so we add the canonical loss to avoid ambiguity in the estimation results:

$$\mathcal{L}_{\text{cano}} = \frac{1}{F \cdot M} \sum_i^F \sum_j^M \|\mathbf{S}_{ij} - \Psi(\hat{\mathbf{R}}_j \mathbf{S}_{ij})\|_l, \quad (12)$$

⁶ It is worth noting that the rotation ambiguity dealt in Theorem 1 is different from the ambiguity in calculating of the corrective transformation matrix [9,8,39,4].

where $\Psi(\cdot)$ is the canonicalization network as C3dpo [28], and $\hat{\mathbf{R}}_j \in SO(3)$ is a randomly sampled rotation for M times across F frames.

Our total loss function is as follows:

$$\mathcal{L} = \mathcal{L}_{\text{data}} + \alpha \mathcal{L}_{\text{norm}} + \lambda \mathcal{L}_{\text{cano}}, \quad (13)$$

where α and λ are trade-off parameters. Our loss functions are all self-supervised, which shares exactly the same setting as the traditional NRSfM methods.

4 Experiments

In this section, we compare our approach with both traditional NRSfM and deep learning-based NRSfM methods.

4.1 Datasets and Setups

CMU MOCAP. For a fair comparison with existing methods, we follow the setup of [41] and choose 9 subjects from 144 subjects of the CMU MOCAP dataset ⁷. We build a training set and testing set following [23], where 80% of the action sequences in each subject are used for training and 20% are used for testing. To verify the robustness, all 3D shapes in the dataset were subjected to a random orthogonal projection to obtain 2D observations, while the coordinates of all 3D shapes in the sequence were centralized in the form of [11]. Thus the camera matrix to be estimated only contains pure rotations. In order to facilitate data input, we first split the motion sequence into multiple chunks according to the subject, and then during training the data are reshuffled in each training round. For evaluation, we use the same criterion as [41] and report the normalized mean 3D error on shapes.

Human3.6M. This is a large dataset containing various types of human motion sequences annotated with 3D ground truth extracted using motion capture systems [20]. Two variants of the dataset are used: the first uses 2D keypoints by orthogonal projection of ground truth 3D keypoint for training and testing (Marked as GT-H36M), and the second uses 2D keypoints detected by HRNet [34] ((Marked as HR-H36M)). For a fair comparison, we follow the evaluation protocol of [24] and evaluate the absolute error measured over 17 joints.

InterHand2.6M This is a large dataset containing various types of hand poses [27]. The 2D annotations in this dataset come from human annotators and 2D keypoint detection network, which is different from the dataset using motion capture to obtain the ground truth of 2D keypoints. Single hand pose motion sequence data (ROM data) are selected for our method evaluation. We collect all single hand ROM data in the 5FPS H+M InterHand2.6M, where 80% are used for training and 20% are used for testing. We evaluate the absolute error measured over 21 joints.

⁷ CMU Motion Capture Dataset. available at <http://mocap.cs.cmu.edu/>

Table 1. Results on the long sequences of the **CMU** motion capture dataset. We follow the comparison in [41]. Ours result surpasses the state-of-the-art on both All and Unseen dataset which is not available during training. **DNRSFM** and **PR-RRN** train a model for each subject separately for testing while we train only one model for different subjects. Notice that many methods have significant gaps in performance on the unseen set versus the training set, while our method achieves consistent performance on both datasets

	Methods	S07	S20	S23	S33	S32	S38	S39	S43	S93	Mean
All	CSF[19]	1.231	1.164	1.238	1.156	1.165	1.188	1.172	1.267	1.117	1.189
	URN[13]	1.504	1.770	1.329	1.205	1.305	1.303	1.550	1.434	1.601	1.445
	CNS[12]	0.310	0.217	0.184	0.177	0.249	0.223	0.312	0.266	0.245	0.243
	C3DPO[28]	0.226	0.235	0.342	0.357	0.354	0.391	0.189	0.351	0.246	0.299
	Ours	0.072	0.122	0.137	0.158	0.142	0.093	0.090	0.108	0.129	0.117
Unseen	DNRSFM	0.097	0.219	0.264	0.219	0.209	0.137	0.127	0.223	0.164	0.184
	PR-RRN	0.061	0.167	0.249	0.254	0.265	0.108	0.028	0.080	0.242	0.162
	C3DPO	0.286	0.361	0.413	0.421	0.401	0.263	0.330	0.491	0.325	0.366
	Ours	0.081	0.139	0.196	0.191	0.195	0.097	0.089	0.139	0.151	0.142

Implementation Details. During the training process for all datasets, we set $\alpha = 0.01$ and $\lambda = 0.003$. For the shape-motion predictor, the feature extraction module f_θ consists of 6 fully connected residual layers with 1024 hidden layer dimensions and output dimensions, and the shape predictor contains 2 fully connected layers, where the input/output dimensions are 1024/10,10/3P. P is the joint number of shape, it relates to the specific dataset. The motion predictor contains one fully connected layer, which has 1024 input sizes and 3 output sizes. In the context layer, the feedforward network f_ϕ is a linear layer with 3P input dimension and 408 output dimension and the head number of attention block is 8, while the feedforward network f_ψ contains 4 fully connected layers with 1024 hidden layer dimensions. The network is trained with the Adam optimizer with an initial learning rate 0.001 and a 10-fold decaying at 1800 update steps and 6400 update steps for the Human3.6M dataset, while the learning weight will decay at 3600 update steps and 9600 update steps for the CMU Mocap dataset.

Table 2. We report the average Normalized Error (NE) as [38] of various methods after training on a mixed-subject(subject 7, 20, 34 and 93) dataset of **CMU**

Methods	Overall	Unseen
C3dpo[28]	0.371	0.364
DNRSFM[23]	0.201	0.219
Ours	0.191	0.203

4.2 NRSfM Results

To guarantee fairness in performance evaluation, we follow the setting in [38] and utilize the same data preprocessing method as C3dpo[28]. We measure the performance of the context on the Human3.6M dataset by calculating the mean per joint position error(**MPJPE**), which is a widely used metric in the literature. To deal with depth flip ambiguity, we follow [24] to evaluate MPJPE for original prediction and depth-flipped prediction, and then retain the lower result.

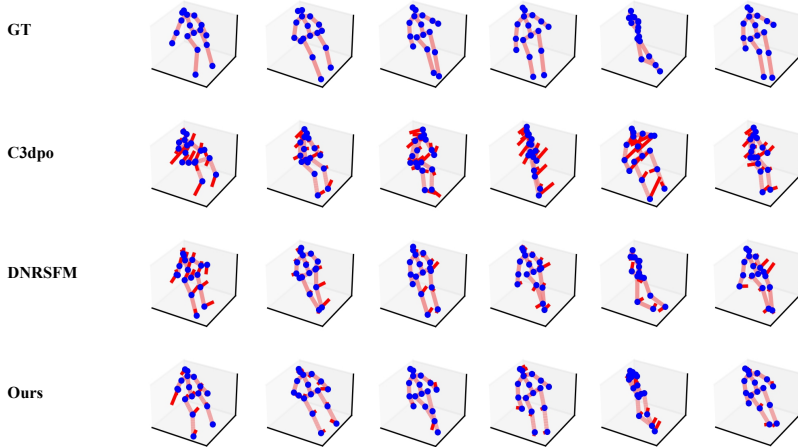


Fig. 3. Qualitative comparison between our method and frame-to-shape method C3dpo [28] and DNRSfM [23] on Human3.6M, where we use the red line to mark the error between the predicted 3D shape and the ground truth 3D shape

In addition, we report the **Stress** metric following [28] on Human3.6M, which is invariant to camera pose and the absolute depth ambiguity. Furthermore, we follow the setting in [41], and utilize the same method as PR-RRN to preprocess the dataset. We use the normalized mean 3D error (e_{3D}) to measure the performance on the CMU MOCAP dataset. The MPJPE, Stress, and e_{3D} metrics are calculated as:

$$\text{MPJPE}(\mathbf{S}_i, \mathbf{S}_i^*) = \frac{1}{P} \sum_{j=1}^P \|\mathbf{S}_{ij} - \mathbf{S}_{ij}^*\| \quad (14)$$

$$\text{Stress}(\mathbf{S}_i, \mathbf{S}_i^*) = \sum_{j < k} \frac{\left| \|\mathbf{S}_{ij} - \mathbf{S}_{ik}\| - \|\mathbf{S}_{ij}^* - \mathbf{S}_{ik}^*\| \right|}{P(P-1)} \quad (15)$$

$$e_{3D}(\mathbf{S}_i, \mathbf{S}_i^*) = \frac{\|\mathbf{S}_i - \mathbf{S}_i^*\|_2}{\|\mathbf{S}_i^*\|_2}, \quad (16)$$

where $\mathbf{S}_{ij}, \mathbf{S}_{ij}^*$ represent the j -th predicted and ground truth joint position coordinate of 3D shape on the i -th frame.

CMU MOCAP. Experimental results on the CMU MOCAP dataset is reported in Table 1. We compare our method with several strong methods. Since we used the same preprocessing method as PR-RRN[41] which achieves state-of-the-art reconstruction accuracy, we directly cite the experiment results from them to compare with our experimental results. The mean reconstruction accuracy of our method on the **Unseen** set exceeds the results reported in PR-RRN

Table 3. Experimental results on the Human3.6M datasets with ground truth 2D keypoint(Marked as GT-H36M) and HRNet detected 2D keypoints(Marked as HR-H36M) and InterHand2.6M(Marked as I26M). We report the mean per joint position error (MPJPE) over the set of test actions. Due to the code of PAUL and PRN are unavailable at the time of testing, we mark the result as ”-”

Methods	GT-H36M		HR-H36M		I26M	
	MPJPE	Stress	MPJPE	Stress	MPJPE	Stress
PRN[30]	86.4	-	-	-	-	-
PAUL[38]	88.3	-	-	-	-	-
C3dpo[28]	95.6	41.5	110.8	56.3	9.8	6.2
DNRSfM[23]	109.9	35.9	121.4	72.4	13.8	8.5
Ours	79.8	33.8	98.1	49.6	8.9	6.1

and surpasses the state-of-the-art result in most of the subjects. Notice that we use a different training strategy from PR-RRN. They train different models for different shape subjects and test them on their respective subjects, while we train only one model and test it on different subjects separately. Also, to ensure the completeness of the control experiments, we have followed our training strategy on a smaller subset CMU Mocap dataset for other methods as Table 2, and the results demonstrate that our method still has advantages. It is worth mentioning that our method shows similar performance on the unseen and training sets, while the performance of other methods is relatively different on these two datasets. In short, our method achieves better reconstruction accuracy while maintaining a significant degree of generalization and reducing training costs.

Human3.6M. Table 3 reports results on Human3.6M with ground truth keypoint and results on Human3.6M with detected keypoints. Our method outperforms other methods by a large margin, and qualitative comparison is shown in Fig. 3 and Fig. 4. We compare our result with several strong deep non-rigid reconstruction methods, where all but PRN [30] use single frame data as input to predict the corresponding 3D shape, and PRN does not impose temporal constraints in the computation. In contrast, our method explicitly models the sequence structure under the temporal constraint, taking advantage of the information ignored by the other methods and thus achieving improved results. We visualize the estimation errors of our method and other methods in Fig. 3.

InterHand2.6M. We also compare our method with several methods on the InterHand2.6M dataset. Quantitative results reported in Table 3 and the visualization results shown in Fig. 4 show that, our method achieves superior 3D reconstruction accuracy in different category of NRSfM task.

4.3 Model Analysis

In this section, we present several ablation studies to validate the ability of our context layer in modeling the sequence structure.

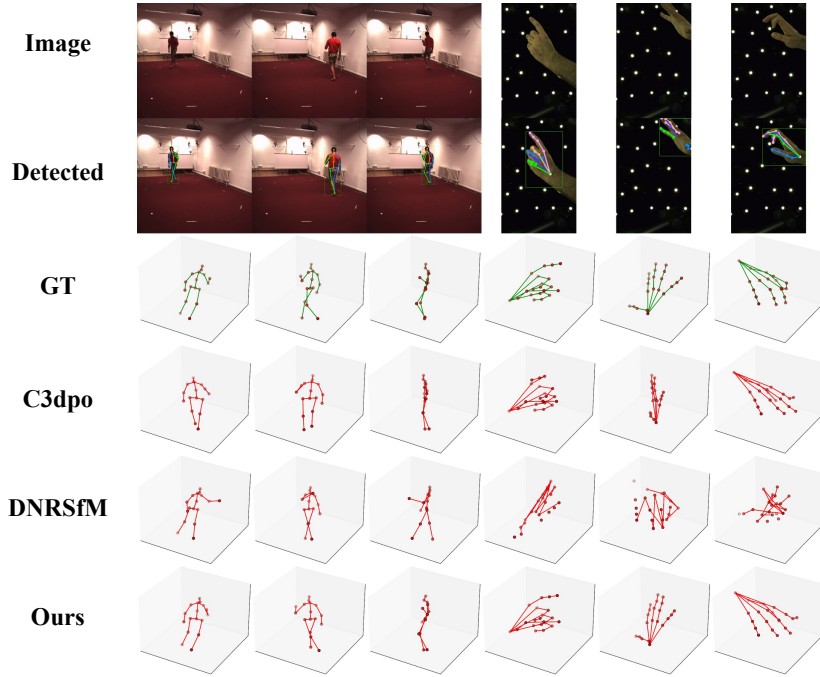


Fig. 4. Visualization of several methods on Human3.6M with detected 2D keypoint and Interhand2.6M dataset

Sequence Modeling To verify the importance of sequence modeling in non-rigid 3D reconstruction, we conducted an experiment by setting the input sequence length of our method to 1 and test it, which makes our method consistent with frame-to-shape methods on experiment setup, and the result is reported in Table 4 (labeled as **single frame**). It can be seen that our method suffers from a significant performance loss after losing the sequence structure information. In turn, it demonstrates the contribution of sequence structural information in deep NRSfM.

We also follow the low-rank assumption for sequences in traditional NRSfM [16] modeling, thus we also design the nuclear norm term as Eq. (10) to constrain the rank of the output shape sequence matrix. To verify its effectiveness, we design an ablation experiment without the nuclear norm term for training. As shown in Table 4, the unconstrained rank of the resulting sequence causes a performance decrease in our results.

To avoid ambiguity in the estimation of non-rigid shapes, we follow C3dpo [28] by introducing canonicalization as a constraint so that no shape in the output sequence can be obtained from a rigid transformation of another shape, ensuring the uniqueness of the inference results. To verify the effectiveness of this constraint, we also conducted ablation experiments, and the results are shown

Table 4. Ablation studies performed on the Human3.6M dataset

Method	MPJPE	Stress
Ours(single frame)	90.7	39.4
Ours(shuffle)	83.7	36.6
Ours(reverse)	80.9	34.5
Ours(4-attention block)	93.6	40.6
Ours(w/o nuclear norm)	81.1	34.7
Ours(w/o canonicalization)	98.1	40.7
Ours	79.8	33.8

in Table 4. The canonicalization loss brings a significant contribution to the improvement of computational accuracy.

A natural thought is if we stack more attention blocks in the context layer, how does this affect our results? To figure out if this would have an impact, we stacked four attention blocks and conducted experiments as Table 4, which proved to have a negative impact instead. Our initial idea is to use attention blocks to obtain self-expressive sequences, but, to do so, only one attention block is sufficient, and adding more blocks may lead to redundant parameters with insufficient constraints, which could make the network fail to converge in the desired direction and lead to the problem of performance degradation.

Temporal Constraint As a sequence-to-sequence deep NRSfM method, our method utilizes the temporal information in different manner as PRN or PR-RRN. We introduce temporal information in our computation, which allows the network to better perceive structural information of the sequences. To verify this, we designed two comparisons: for a trained model, we input a set of disrupted the order of the input sequences and reversed the order of the input sequences and compared their respective results with those of the normal input. The results are shown in Table 4 (labeled as shuffle and reverse). Inverting the input sequence does not change the continuity of the sequence, so it does not have much impact on the estimation accuracy, while completely disrupting the input order destroys the original continuity of the sequences, which has a drastic impact on our results.

5 Conclusions

In this paper, we have proposed a novel sequence-to-sequence translation perspective to deep NRSfM, where the input 2D sequence is taken as a whole to reconstruct the 3D deforming shape sequence. Our framework consists of a shape-motion predictor module and a context modeling module. We utilized a self-expressiveness mechanism and temporal position encoding to characterize complex non-rigid motion. Our method naturally combines the best of two worlds, *i.e.*, the representation learning ability of deep neural networks and the geometric modeling ability of the conventional optimization framework. Experiments across different datasets (CMU Mocap, Human3.6M, InterHand) demonstrate the superiority of our method over both traditional and deep NRSfM methods.

References

1. Agudo, A.: Unsupervised 3d reconstruction and grouping of rigid and non-rigid categories. *IEEE Trans. Pattern Anal. Mach. Intell. (PAMI)* **44**(1), 519–532 (2020) [3](#)
2. Agudo, A., Moreno-Noguer, F.: Recovering pose and 3d deformable shape from multi-instance image ensembles. In: *In Proc. of the Asian Conf. on Computer Vision (ACCV)*. pp. 291–307 (2016) [3](#)
3. Agudo, A., Moreno-Noguer, F.: Robust spatio-temporal clustering and reconstruction of multiple deformable bodies. *IEEE Trans. Pattern Anal. Mach. Intell. (PAMI)* **41**(4), 971–984 (2018) [2](#)
4. Akhter, I., Sheikh, Y., Khan, S.: In defense of orthonormality constraints for non-rigid structure from motion. In: *IEEE Conf. Comput. Vis. Pattern Recog. (CVPR)*. pp. 1534–1541 (2009) [8](#)
5. Akhter, I., Sheikh, Y., Khan, S., Kanade, T.: Nonrigid structure from motion in trajectory space. In: *Adv. Neural Inform. Process. Syst. (NeurIPS)*. pp. 41–48 (2008) [1](#), [3](#)
6. Baevski, A., Zhou, H., Mohamed, A., Auli, M.: wav2vec 2.0: A framework for self-supervised learning of speech representations. In: *Adv. Neural Inform. Process. Syst. (NeurIPS)*. pp. 12449–12460 (2020) [4](#)
7. Bai, Z., Cui, Z., Rahim, J.A., Liu, X., Tan, P.: Deep facial non-rigid multi-view stereo. In: *IEEE Conf. Comput. Vis. Pattern Recog. (CVPR)*. pp. 5850–5860 (2020) [4](#)
8. Brand, M.: A direct method for 3d factorization of nonrigid motion observed in 2d. In: *IEEE Conf. Comput. Vis. Pattern Recog. (CVPR)*. pp. 122–128 (2005) [8](#)
9. Brand, W.: Morphable 3d models from video. In: *Proceedings of the 2001 IEEE Computer Society Conference on Computer Vision and Pattern Recognition. CVPR 2001*. pp. 456–463 (2001) [8](#)
10. Brannen, C.: Linear subspaces of rotation matrices. available at <https://math.stackexchange.com/q/98628> (2012) [18](#)
11. Bregler, C., Hertzmann, A., Biermann, H.: Recovering non-rigid 3d shape from image streams. In: *IEEE Conf. Comput. Vis. Pattern Recog. (CVPR)*. pp. 690–696 (2000) [1](#), [3](#), [5](#), [9](#)
12. Cha, G., Lee, M., Cho, J., Oh, S.: Reconstruct as far as you can: Consensus of non-rigid reconstruction from feasible regions. *IEEE Trans. Pattern Anal. Mach. Intell. (PAMI)* **43**(2), 623–637 (2019) [10](#)
13. Cha, G., Lee, M., Oh, S.: Unsupervised 3d reconstruction networks. In: *Int. Conf. Comput. Vis. (ICCV)*. pp. 3849–3858 (2019) [2](#), [10](#)
14. Choi, J., Gao, C., Messou, C.E.J., Huang, J.B.: Why can’t i dance in the mall? learning to mitigate scene bias in action recognition. In: *Adv. Neural Inform. Process. Syst. (NeurIPS)*. pp. 853–865 (2019) [4](#)
15. Dai, Y., Deng, H., He, M.: Dense non-rigid structure-from-motion made easy—a spatial-temporal smoothness based solution. In: *IEEE Int. Conf. Image Process. (ICIP)*. pp. 4532–4536 (2017) [2](#)
16. Dai, Y., Li, H., He, M.: A simple prior-free method for non-rigid structure-from-motion factorization. *Int. J. Comput. Vis. (IJCV)* **107**(2), 101–122 (2014) [2](#), [3](#), [8](#), [13](#)
17. Devlin, J., Chang, M.W., Lee, K., Toutanova, K.: Bert: Pre-training of deep bidirectional transformers for language understanding. *arXiv preprint arXiv:1810.04805* (2018) [7](#)

18. Garg, R., Roussos, A., Agapito, L.: Dense variational reconstruction of non-rigid surfaces from monocular video. In: IEEE Conf. Comput. Vis. Pattern Recog. (CVPR). pp. 1272–1279 (2013) [3](#)
19. Gotardo, P.F., Martinez, A.M.: Computing smooth time trajectories for camera and deformable shape in structure from motion with occlusion. IEEE Trans. Pattern Anal. Mach. Intell. (PAMI) **33**(10), 2051–2065 (2011) [1](#), [10](#)
20. Ionescu, C., Papava, D., Olaru, V., Sminchisescu, C.: Human3.6m: Large scale datasets and predictive methods for 3d human sensing in natural environments. IEEE Trans. Pattern Anal. Mach. Intell. (PAMI) **36**(7), 1325–1339 (2014) [9](#)
21. Ji, P., Zhang, T., Li, H., Salzmann, M., Reid, I.: Deep subspace clustering networks. Adv. Neural Inform. Process. Syst. (NeurIPS) **30**, 24–33 (2017) [2](#), [6](#), [7](#)
22. Kocabas, M., Athanasiou, N., Black, M.J.: Vibe: Video inference for human body pose and shape estimation. In: IEEE Conf. Comput. Vis. Pattern Recog. (CVPR). pp. 5253–5263 (2020) [4](#)
23. Kong, C., Lucey, S.: Deep non-rigid structure from motion with missing data. IEEE Trans. Pattern Anal. Mach. Intell. (PAMI) **43**(12), 4365–4377 (2021) [2](#), [4](#), [9](#), [10](#), [11](#), [12](#)
24. Kudo, Y., Ogaki, K., Matsui, Y., Odagiri, Y.: Unsupervised adversarial learning of 3d human pose from 2d joint locations. In: Eur. Conf. Comput. Vis. (ECCV) (2018) [9](#), [10](#)
25. Kumar, S., Dai, Y., Li, H.: Multi-body non-rigid structure-from-motion. In: In Proc. of the International Conf. on 3D Vision (3DV). pp. 148–156 (2016) [3](#), [5](#), [6](#)
26. Kumar, S., Dai, Y., Li, H.: Spatio-temporal union of subspaces for multi-body non-rigid structure-from-motion. Pattern Recognition(PR) **71**, 428–443 (2017) [3](#)
27. Moon, G., Yu, S.I., Wen, H., Shiratori, T., Lee, K.M.: Interhand2. 6m: A dataset and baseline for 3d interacting hand pose estimation from a single rgb image. In: Eur. Conf. Comput. Vis. (ECCV). pp. 548–564 (2020) [9](#)
28. Novotny, D., Ravi, N., Graham, B., Neverova, N., Vedaldi, A.: C3dpo: Canonical 3d pose networks for non-rigid structure from motion. In: Int. Conf. Comput. Vis. (ICCV). pp. 7688–7697 (2019) [2](#), [4](#), [8](#), [9](#), [10](#), [11](#), [12](#), [13](#)
29. Park, S., Lee, M., Kwak, N.: Procrustean regression: A flexible alignment-based framework for nonrigid structure estimation. IEEE Trans. Image Process. (TIP) **27**(1), 249–264 (2017) [4](#)
30. Park, S., Lee, M., Kwak, N.: Procrustean regression networks: Learning 3d structure of non-rigid objects from 2d annotations. In: Eur. Conf. Comput. Vis. (ECCV). pp. 1–18 (2020) [4](#), [12](#)
31. Radford, A., Narasimhan, K., Salimans, T., Sutskever, I.: Improving language understanding by generative pre-training. URL https://s3-us-west-2.amazonaws.com/openai-assets/research-covers/language-unsupervised/language_understanding_paper.pdf (2018) [7](#)
32. Sidhu, V., Tretschk, E., Golyanik, V., Agudo, A., Theobalt, C.: Neural dense non-rigid structure from motion with latent space constraints. In: Eur. Conf. Comput. Vis. (ECCV). pp. 204–222 (2020) [4](#)
33. Simon, T., Valmadre, J., Matthews, I., Sheikh, Y.: Kronecker-markov prior for dynamic 3d reconstruction. IEEE Trans. Pattern Anal. Mach. Intell. (PAMI) **39**(11), 2201–2214 (2017) [1](#), [3](#)
34. Sun, K., Xiao, B., Liu, D., Wang, J.: Deep high-resolution representation learning for human pose estimation. In: IEEE Conf. Comput. Vis. Pattern Recog. (CVPR). pp. 5693–5703 (2019) [9](#)

35. Sutskever, I., Vinyals, O., Le, Q.V.: Sequence to sequence learning with neural networks. In: *Adv. Neural Inform. Process. Syst. (NeurIPS)*. p. 3104–3112 (2014) [4](#)
36. Torresani, L., Hertzmann, A., Bregler, C.: Nonrigid structure-from-motion: Estimating shape and motion with hierarchical priors. *IEEE Trans. Pattern Anal. Mach. Intell. (PAMI)* **30**(5), 878–892 (2008) [3](#)
37. Wang, C., Lin, C.H., Lucey, S.: Deep nrsfm++: Towards 3d reconstruction in the wild. In: *In Proc. of the International Conf. on 3D Vision (3DV)*. pp. 12–22 (2020) [4](#)
38. Wang, C., Lucey, S.: Paul: Procrustean autoencoder for unsupervised lifting. In: *IEEE Conf. Comput. Vis. Pattern Recog. (CVPR)*. pp. 434–443 (2021) [4](#), [10](#), [12](#)
39. Xiao, J., Chai, J.x., Kanade, T.: A closed-form solution to non-rigid shape and motion recovery. In: *Eur. Conf. Comput. Vis. (ECCV)*. pp. 573–587 (2004) [3](#), [8](#)
40. Xu, X., Dunn, E.: Gtt-net: Learned generalized trajectory triangulation. In: *Int. Conf. Comput. Vis. (ICCV)*. pp. 5795–5804 (2021) [4](#)
41. Zeng, H., Dai, Y., Yu, X., Wang, X., Yang, Y.: Pr-rrn: Pairwise-regularized residual-recursive networks for non-rigid structure-from-motion. In: *Int. Conf. Comput. Vis. (ICCV)*. pp. 5600–5609 (2021) [4](#), [9](#), [10](#), [11](#)
42. Zhang, T., Ji, P., Harandi, M., Huang, W., Li, H.: Neural collaborative subspace clustering. In: *In Proc. of the International Conf. on Machine learning (ICML)*. pp. 7384–7393 (2019) [2](#)
43. Zhang, Z., Shi, Y., Yuan, C., Li, B., Wang, P., Hu, W., Zha, Z.: Object relational graph with teacher-recommended learning for video captioning. In: *IEEE Conf. Comput. Vis. Pattern Recog. (CVPR)*. pp. 13275–13285 (2020) [4](#)
44. Zhu, Y., Huang, D., De La Torre, F., Lucey, S.: Complex non-rigid motion 3d reconstruction by union of subspaces. In: *IEEE Conf. Comput. Vis. Pattern Recog. (CVPR)*. pp. 1542–1549 (2014) [1](#), [2](#), [3](#), [5](#), [6](#)

Deep Non-rigid Structure-from-Motion: A Sequence-to-Sequence Translation Perspective

(Supplementary Materials)

Abstract. In this supplementary material, we firstly provide a complete proof of Theorem 1 in Section 3.5 of the main paper. The whole proof mainly consists of mathematical induction and simple matrix operations. Secondly, we show the performance of our model in inference on input sequences of different lengths.

A Proof of Theorem 1

Theorem 1. *Suppose that a deformable shape $\mathbf{S}^\# \in \mathbb{R}^{3F \times P}$ lies in a low-rank space, then we have:*

$$\text{rank}(g(\mathbf{S})) \leq \text{rank}(g(\mathbf{Q}^{-1}\mathbf{S})). \quad (1)$$

The equal sign holds if and only if \mathbf{Q} contains only one rotation component $\mathbf{Q}_1 = \dots = \mathbf{Q}_F$, i.e., a global rotation on all the frames.

In this section, we provide a detailed proof of Theorem 1. Before that, we expound a conclusion about the rotation matrix in $SO(3)$, then present the notation and preliminary.

Lemma 1. *There are nine basis rotation matrices that are linearly independent and can represent any rotation matrix in $SO(3)$ linearly [10].*

Proof. First, we define three “signed permutation” matrices. For $x, y, z \in \mathbb{R}$, let

$$\begin{aligned} \mathbf{M}_1(x, y, z) &= \begin{bmatrix} x & y & -z \\ y & z & -x \\ z & x & -y \end{bmatrix}, \\ \mathbf{M}_2(x, y, z) &= \begin{bmatrix} -y & z & x \\ -z & x & y \\ -x & y & z \end{bmatrix}, \\ \mathbf{M}_3(x, y, z) &= \begin{bmatrix} z & -x & y \\ x & -y & z \\ y & -z & x \end{bmatrix}. \end{aligned} \quad (2)$$

For any matrix $\mathbf{R} = (r_{ij})_{1 \leq i, j \leq 3}$, we have $\mathbf{R} = (\mathbf{R}_1 + \mathbf{R}_2 + \mathbf{R}_3)/2$, where:

$$\begin{aligned}\mathbf{R}_1 &= \mathbf{M}_1(r_{11} + r_{32}, r_{12} + r_{21}, r_{22} + r_{31}) \\ &= (r_{11} + r_{32})\mathbf{M}_1(1, 0, 0) + (r_{12} + r_{21})\mathbf{M}_1(0, 1, 0) \\ &\quad + (r_{22} + r_{31})\mathbf{M}_1(0, 0, 1), \\ \mathbf{R}_2 &= \mathbf{M}_2(r_{13} + r_{22}, r_{23} + r_{32}, r_{12} + r_{33}) \\ &= (r_{13} + r_{22})\mathbf{M}_2(1, 0, 0) + (r_{23} + r_{32})\mathbf{M}_2(0, 1, 0) \\ &\quad + (r_{12} + r_{33})\mathbf{M}_2(0, 0, 1), \\ \mathbf{R}_3 &= \mathbf{M}_3(r_{21} + r_{33}, r_{13} + r_{31}, r_{11} + r_{23}) \\ &= (r_{21} + r_{33})\mathbf{M}_1(1, 0, 0) + (r_{13} + r_{31})\mathbf{M}_3(0, 1, 0) \\ &\quad + (r_{11} + r_{23})\mathbf{M}_3(0, 0, 1).\end{aligned}$$

Now, all the nine matrices $\mathbf{M}_k(1, 0, 0)$, $\mathbf{M}_k(0, 1, 0)$, $\mathbf{M}_k(0, 0, 1)$, $1 \leq k \leq 3$ lie in $SO(3)$, and they form a basis of any rotation matrix.

Notation. We define the per-frame rotation ambiguity as $\mathbf{Q} = \text{blkdiag}(\mathbf{Q}_1, \dots, \mathbf{Q}_F)$ in Theorem 1. But for the simplification of proof, we rewrite the rotation ambiguity \mathbf{Q}^{-1} acting on \mathbf{S} as $\mathbf{R} = \text{blkdiag}(\mathbf{R}_1, \dots, \mathbf{R}_F) \in \mathbb{R}^{3F \times 3F}$. Then we straighten the rows of each per-frame rotation matrix \mathbf{R}_i and form the new expression \mathbf{R}^\sharp as follow:

$$\mathbf{R}^\sharp = \text{diag}(\overline{vec}(\mathbf{R}_1)', \dots, \overline{vec}(\mathbf{R}_F)')_{F \times 9F}, \quad (3)$$

where \overline{vec} denotes the row-straightening operator. The reshuffled shape \mathbf{S}^\sharp can be represented as:

$$\mathbf{S}_*^\sharp = \mathbf{R}^\sharp \hat{\mathbf{B}} = \mathbf{R}^\sharp \begin{bmatrix} \mathbf{B}_{11} & \cdots & \mathbf{B}_{1P} \\ \vdots & \ddots & \vdots \\ \mathbf{B}_{F1} & \cdots & \mathbf{B}_{FP} \end{bmatrix} \quad (4)$$

where $\hat{\mathbf{B}}$ is a block matrix formed by the elements of shape \mathbf{S} . We assume that the j -th feature point coordinates of the i -th frame image are (x_j^i, y_j^i, z_j^i) , then $\mathbf{B}_{ij} \in \mathbb{R}^{9 \times 3}$ can be denoted as:

$$\mathbf{B}_{ij} = \begin{bmatrix} x_j^i & y_j^i & z_j^i & & & \\ & x_j^i & y_j^i & z_j^i & & \\ & & x_j^i & y_j^i & z_j^i & \\ & & & x_j^i & y_j^i & z_j^i \end{bmatrix}^T$$

Preliminary. $K \ll F$ and \mathbf{S}^\sharp is strict-rank K .

$K \ll F$ is a natural assumption based on the low-rank condition. Then we introduce the definition of strict-rank.

Definition 1. A rank K matrix \mathbf{S}^\sharp is non-strict-rank K if \mathbf{S}^\sharp satisfies the following condition after taking away any f rows:

$$\text{rank}((\mathbf{S}^\sharp)') < K, \text{ and, } f/F < \varepsilon$$

Here, $(\mathbf{S}^\sharp)'$ is the new matrix after taking away f rows, and ε is a small scalar. F is the number of rows of \mathbf{S}^\sharp .

If shape \mathbf{S} is non-strict-rank, we can remove just a few frames of it and reach a lower rank shape structure. We focus on strict-rank K shape here and do not discuss this degenerate form. The condition that \mathbf{S}^\sharp is strict-rank K means that, there are multiple maximally independent groups in the rows of \mathbf{S} . Because $K \ll F$, we can assume that the number of maximally independent groups is more than 9. Notice that when the rank of \mathbf{S}^\sharp is K , the rank of $\hat{\mathbf{B}}$ should be $9K$. After introducing the preconditions, we prove Theorem 1 as below.

Proof. We use induction to expound the conclusion. From Eq. (4), \mathbf{S}_*^\sharp can be rewritten in a new form,

$$\mathbf{S}_*^\sharp = \begin{bmatrix} \overline{vec}(\mathbf{R}_1)' \mathbf{B}_{11} & \overline{vec}(\mathbf{R}_1)' \mathbf{B}_{12} & \cdots & \overline{vec}(\mathbf{R}_1)' \mathbf{B}_{1P} \\ \overline{vec}(\mathbf{R}_2)' \mathbf{B}_{21} & \overline{vec}(\mathbf{R}_2)' \mathbf{B}_{22} & \cdots & \overline{vec}(\mathbf{R}_2)' \mathbf{B}_{2P} \\ \vdots & \vdots & \ddots & \vdots \\ \overline{vec}(\mathbf{R}_F)' \mathbf{B}_{F1} & \overline{vec}(\mathbf{R}_F)' \mathbf{B}_{F2} & \cdots & \overline{vec}(\mathbf{R}_F)' \mathbf{B}_{FP} \end{bmatrix} \quad (5)$$

We use mathematical induction for the number of rotation components in ambiguity matrix, and divide the whole proof into three parts.

1. When \mathbf{R}^\sharp has only one rotation component, *i.e.*, $\mathbf{R}_1 = \mathbf{R}_2 = \cdots = \mathbf{R}_F$, we have $rank(\mathbf{S}_*^\sharp) = K$. This situation is equal to global ambiguity, which is always estimated before optimization.

This conclusion is obvious. We rewrite the matrix $\hat{\mathbf{B}}$ as $[\hat{\mathbf{B}}_1^T, \cdots, \hat{\mathbf{B}}_F^T]^T$. Based on the analysis in Definition 1, we assume that the first $9K$ rows of $\hat{\mathbf{B}}$ are a maximally independent groups. For any row $\mathbf{s}_j^\sharp (j > K)$ of \mathbf{S}_*^\sharp , it can be composed of the first K rows of \mathbf{S}_*^\sharp *i.e.*,

$$\exists \vec{\alpha} \neq \vec{0}, \overline{vec}(\mathbf{R}_1)' \hat{\mathbf{B}}_j = \overline{vec}(\mathbf{R}_1)' \sum_{i=1}^K \alpha_i \hat{\mathbf{B}}_i \quad (6)$$

Because $\hat{\mathbf{B}}_1, \cdots, \hat{\mathbf{B}}_K$ are a maximally independent group of $\hat{\mathbf{B}}$.

2. When \mathbf{R}^\sharp has s rotation components $\mathbf{R}_1, \mathbf{R}_2, \cdots, \mathbf{R}_s$, we have $rank(\mathbf{S}_*^\sharp) > K$.

First, we reveal that $(s-1)K < rank(\mathbf{S}_*^\sharp) \leq sK$ when $s \leq 9$. Without loss of generality, we assume that these s components of rotation are linearly independent of each other. According to proof step 1, this conclusion is true when $s = 1$. Suppose that conclusion is true if $s \leq n < 9$, we prove it the same when $s = n + 1$. Based on our assumption, there are many maximally independent groups in $\hat{\mathbf{B}}$, which means any rotation components $\overline{vec}(\mathbf{R}_i)', i \leq n$ can multiply with at least a maximally independent group. We assume that label set $\{i_j\}, j = 1, \cdots, nK$ corresponds to K -dimensional maximally independent groups containing n rotation components. Then we introduce the $(n+1)th$ rotation component cannot be composed of these

$n \times k$ vectors.

$$\begin{aligned} \sum_{j=1}^K \alpha_j \overline{vec}(\mathbf{R}_1)' \hat{\mathbf{B}}_{i_j} + \cdots + \sum_{j=(n-1)K+1}^{nK} \alpha_j \overline{vec}(\mathbf{R}_1)' \hat{\mathbf{B}}_{i_j} \\ = \overline{vec}(\mathbf{R}_{n+1})' \hat{\mathbf{B}}_c \end{aligned} \quad (7)$$

Suppose that there are non-zero vector $\vec{\alpha}$ for Eq. (7) to be true. Because $\{\hat{\mathbf{B}}_i\}_{i=1}^K$ is a maximally independent group, we rewrite Eq. (7) by using these groups to present any block $\hat{\mathbf{B}}$ in it.

$$\begin{aligned} \sum_{j=1}^K (\gamma_j^1 \overline{vec}(\mathbf{R}_1)' + \cdots + \gamma_j^n \overline{vec}(\mathbf{R}_n)') \hat{\mathbf{B}}_{i_j} \\ = \sum_{j=1}^K \beta_j \overline{vec}(\mathbf{R}_{n+1})' \hat{\mathbf{B}}_{i_j} \end{aligned} \quad (8)$$

where, γ_j^i, β_j are coefficients. Because these rotations $\mathbf{R}_1, \dots, \mathbf{R}_{n+1}$ are independent, they are not linear dependent with each other and Eq. (8) is not true. So $\overline{vec}(\mathbf{R}_{n+1})' \hat{\mathbf{B}}_c$ is linearly independent of these $n \times k$ basis vectors in the left of Eq. (7), *i.e.*, $nK < \text{rank}(\mathbf{S}_*^\sharp)$. If there are enough $\overline{vec}(\mathbf{R}_{n+1})'$ in \mathbf{R}^\sharp , we can find another set of linearly independent vectors:

$$\sum_{j=nK+1}^{(n+1)K} \alpha_j \overline{vec}(\mathbf{R}_{n+1})' \hat{\mathbf{B}}_{i_j}, \quad (9)$$

which means the maximum rank of \mathbf{S}_*^\sharp is $(n+1)K$. By mathematical induction, we have proved the conclusion of $(s-1)K < \text{rank}(\mathbf{S}_*^\sharp) \leq sK$ when $s \leq 9$. Then, if $s > 9$, the rank of \mathbf{S}_*^\sharp should be $9K$. This is because Eq. (8) can be true when $s > 9$, so the rank of \mathbf{S}_*^\sharp can not increase with the augment of s .

3. Finally, we discuss a more general situation, *i.e.*, $\mathbf{R}_1, \mathbf{R}_2, \dots, \mathbf{R}_F$ are almost entirely different. According to proof step 2, we can easily conclude that the rank of \mathbf{S}_*^\sharp in Eq. (5) is $9K$. A basis of \mathbf{S}_*^\sharp can be found by the way below. For any row of \mathbf{S}_*^\sharp , we can use the maximally independent group of $\hat{\mathbf{B}}$ and $SO(3)$ to represent:

$$\begin{aligned} \overline{vec}(\mathbf{R}_c)' \hat{\mathbf{B}}_c &= \sum_{j=1}^K \alpha_j \overline{vec}(\mathbf{R}_c)' \hat{\mathbf{B}}_{i_j} \\ &= \sum_{j=1}^K \alpha_j \sum_{n=1}^9 \beta_n \overline{vec}(\mathbf{R}_n)' \hat{\mathbf{B}}_{i_j} \\ &= \sum_{j=1}^K \sum_{n=1}^9 \gamma_{jn} \overline{vec}(\mathbf{R}_n)' \hat{\mathbf{B}}_{i_j} \end{aligned} \quad (10)$$

Based on the proof above, we can conclude that the rank of the reshuffled shape $\mathbf{S}^\#$ will increase when rotation ambiguity exists (except for the global ambiguity).

B Input Length Analysis

Within our sequence-to-sequence reconstruction framework, we take the whole sequence as input rather than a single frame. Here, we conduct experiments to study the robustness of our method to the input length. To this end, we train our model with 32 frames as inputs' length for 15 and 180 epochs, whereas, we use different lengths in the test stage to investigate the robustness.

As shown in Fig. 1, a higher number of training epochs gives better results when the length of the input sequence at test time is the same as training. Moreover, when the test sequence length is shorter than the training sequence, the test accuracy decreases gradually with the reduction of the sequence length. However, when the test sequence length is longer than the training sequence, we can clearly observe that the degradation of the test accuracy as the test sequence grows. It should also be noted that when the number of training rounds is relatively small, the accuracy degradation due to the change in input length is less dramatic compared with the case where the number of training epochs is large.

We conjecture that this phenomenon stems from our learnable positional encoding. The maximum length that can be learned by the learnable positional encoding is limited by the length of the training sequences, which prevents the position relations of excessively long test sequences from being expressed correctly and causes drastic degradation of the results. Conversely, if the test sequences are shorter than the training sequences, then they do not cause similar problems, but they also have some impact on the estimation results due to the reduction of the sequence context information. Moreover, when the number of training rounds is less, the learnable positional encoding is not able to fully encode the temporal relationship of the sequence, which makes the network less sensitive to changes in the input sequence length. At the same time, there is no way to obtain higher estimation accuracy. Therefore, a higher number of training epochs, although bringing higher estimation accuracy, also makes the network more sensitive to changes in the input sequence length.

It can be seen that our method is able to cope with a range of inputs of various length sequences after the training is completed. However, our limitation is that our method suffers from failure if this sequence is longer than our training sequence, so future work can be centered here to investigate how to improve the robustness of the network against input sequences with different length while ensuring high enough accuracy.

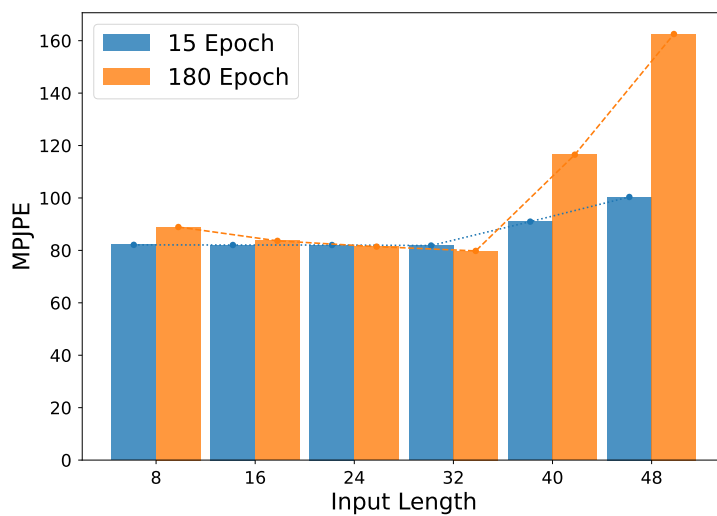


Fig. 1. Experimental results on the Human3.6M dataset. We report the estimation accuracy for different input sequence lengths under the two models.